V CIRP Conference on Biomanufacturing

Analytical modeling of micro-milling operations on biocompatible Ti6Al4V titanium alloy

Andrea Abeni[a*], Cristian Cappellini[b], Paola Serena Ginestra[a], Aldo Attanasio[a]

[a]*University of Brescia, Department of Mechanical and Industrial Engineering, V. Branze 38, Brescia 25123, Italy*
[b]*Free University of Bolzano, Faculty of Science and Technology, Piazza Università 5, Bolzano 39100, Italy*

* Corresponding author. Tel. 030 3715712; fax: 030 3712448. *E-mail address:* andrea.abeni@unibs.it

Abstract

Among the biocompatible materials, Ti6Al4V titanium alloy is widely spread due to its properties, such as corrosion and fatigue resistance combined with low density. Ti6Al4V can be processed by Additive Manufacturing technologies, such as Power Bed Fusion (PBF). The biomedical applications require good surface finishing to ensure biocompatibility with tissues and organs. Machining is an adequate process to ensure low final roughness of components. The necessity to realize miniaturized features implicates the usage of micro mills with diameter lower than one millimeter. It implicates several issues, such as size effects, higher than expected cutting forces, rapid tool wear which can be addressed by experimental tests and process modeling. This work reports the results of micro-milling performed on additively manufactured samples in Ti6Al4V. PBF process was utilized to manufacture the samples by employing laser source (PBF-LB). The machining center was equipped with a loadcell to acquire cutting force signal. An analytical cutting force model was calibrated on the experimental data with the purpose of predicting loads on the tool by considering ploughing- and shearing- regimes. Specific machining tests were performed to calculate the Minimum Uncut Chip Thickness (MUCT) and to calibrate the unknow parameters of the model, while further tests allowed to verify the reliability of the model about the cutting force prediction. The elaboration of the cutting force data was performed by an iterative methodology based on the Particle Swarm Optimization (PSO) algorithm.

Keywords: Biomanufacturing; Ti6Al4V alloy; Micro machining.

1. Introduction

The mechanical properties of a part produced by Powder Bed Fusion (PBF) are directly related with the impact that the process has on the residual stresses and metallurgical state. A crucial aspect is, in fact, the optimization of the parameters that each PBF process is taking into account. Another aspects that is highly influenced, and therefore deeply analyzed as an outcome of these processes, is the surface quality of the final parts [1]. Complex and convoluted parts resulting from Additive Manufacturing of metals are always characterized by poor surface finishing and integrity. Considering the high impact of the surface quality on the final performances and

applications of metal parts, the most used PBF processes such as Laser-Based (PBF-LB) and Electron-Beam-Based (PBF-BB) are frequently investigated in relation to machining procedures that can be applied to improve the surface properties of PBF samples. [2, 3] Precisely, the PBF process optimization strategies highlighted in the up-to-date literature, are not showing a possible way to control and predict the surface features of the samples demonstrating the lack of information on the direct relation between process input parameters and surface aspects [4]. Further, PBF specimens are also characterized by internal porosities that require the application of Hot Isostatic Pressuring to assure the proper density of the parts. The necessity of different post-processing

steps to improve the overall properties of these samples is a general drawback of the metals produced by additive layer manufacturing. PBF parts can be suitable for several applications that benefit of complex, tailored and customized geometries for the optimization of different aspects such as the energy absorption, fatigue properties, heat exchange and biomedical outcomes [5, 6]. For example, the Ti6Al4V (Ti64) titanium alloy is extensively use for biomedical implants production due to the excellent properties of this metal [7]. This material has been widely produced with PBF technologies, especially Laser Based techniques, leading to a big advance in the personalized medicine field. Besides, the biomechanical outcomes of an implant are highly influenced by the corrosion and fatigue properties that, on the other side, are subsequential of the surface properties and integrity. Thus, the biocompatibility and load bearing performances of a metal implant, crucial for the right outcome of the surgery, are dependent on the surface defects deriving from the PBF processes followed by finishing or passivation. In fact, biological activity promoted by a proper implant is directly related to the stress concentration and bioactivity of the natural tissue that cannot be altered by the poor surface quality of the samples.

One of the most used and standard process for the obtainment of high-resolution surfaces is milling, especially micro milling, considering the efficiency of micro tools on complex geometries and micro features [8, 9]. However, the microstructure of the machined material has an important effect on the micro milling operations. For this reason, the process parameters need to be optimized depending on the material that requires the micro machining process. Considering the high cooling rates typical of the PBF-LB process, the microstructure of Ti64 usually demonstrate a dominant martensitic microstructure although the β phase remains the primary mode of solidification as expected for Ti64 alloys [10-12].

A crucial aspect of the micro milling process is the identification of the Minimum Uncut Chip Thickness (MUCT), comparable to the cutting edge radius of the selected tool. This value provides the transition from an elasto-plastic regime (shearing) to a deformation of the material that leads to an incorrect chip formation (ploughing). The MUCT quantification assures the quality of the finished parts as allows the identification of the right deformation regime and thus the cutting force and variation of cutting energy of the transition from ploughing to shearing, which is the desired regime since it does not affect the surface properties and accuracy of the treated samples [13]. To fully evaluate the machining process, the cutting speed has to be analyzed with the effects of tools run-out that may alter the cutting loads [14, 15]. Moreover, the cutting force during milling of Ti64 typically decreases with the increasing of the cutting speed.

This work aims to study the micro milling process of Ti64 produced by PBF-LB technique providing a critical evaluation of the material removal behavior resulting at constant cutting speed. Cubical PBF-LB samples have been machined by tungsten carbide coated micro end mills. Firstly, the cutting force has been acquired and specific forces computed, considering the feed per tooth, to identify the passage from

ploughing. Furthermore, the cutting speed effect has been investigated to evaluate the impact on the cutting forces.

2. The Analytical Cutting Force Model

The analytical cutting force model proposed in this work can estimate the cutting force by contemplating both ploughing and shearing regimes. Under the hypothesis of negligibility of the axial force module and tool deflection during micro-milling, the two-dimensional cutting model, reported in Fig. 1, can be analyzed as a reference configuration.
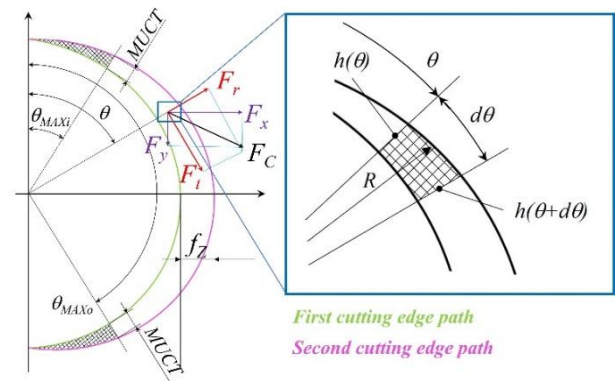

Fig. 1. Two-dimensional representation of micro-milling process.

From Fig. 1 it is possible to observe that the value of instantaneous chip thickness $h(\theta)$ [mm] varies as a function of the rotation angle θ of the mill, and of the employed feed per tooth f_Z, by equation (1):

$$h(\theta) = f_z \cdot sin(\theta) \tag{1}$$

The cutting area A_C can be calculated as the evolution of $h(\theta)$, as reported in equation (2):

$$A_c(\theta) = \int_0^\theta \left(\frac{h(\theta)+h(\theta+d\theta)}{2}\right) R \, d\theta \tag{2}$$

Where R is the radius of the mill and $d\theta$ is the infinitesimal variation of the tool rotation angle.

Tangential F_t and radial F_r components of the cutting force F_C can be determined by defining specific forces parameters for the shearing and ploughing regimes. Considering K_{ts} and K_{rs} as specific force coefficients for the shearing regime in tangential and radial directions [N/mm²] respectively, while K_{tp} and K_{rp} as the coefficients for the ploughing regime in tangential and radial directions [N/mm³] respectively, it is possible to estimate F_t and F_r by the set of equations (3):

$$F_t(\theta) = \left(K_{ts} \cdot h(\theta) + K_{tp} \cdot A_p(\theta)\right) \cdot a_p$$
$$F_r(\theta) = \left(K_{rs} \cdot h(\theta) + K_{rp} \cdot A_p(\theta)\right) \cdot a_p \tag{3}$$

Where $A_p(\theta)$ is the ploughed area [mm²], and a_p is the axial depth of cut [mm]. $A_p(\theta)$ is determined as the area covered by the milling cutter edge up to the value of θ reaches θ_{MAXi}. At

this angle, h is equal to MUCT and the amount of ploughed area A_{pMAX} is attained. Above θ_{MAXi} the ploughed area remains constant until h reduces again below MUCT, in correspondence of θ_{MAXo}, in the ending section of the cut while the tool is disengaging. This behavior of $A_p(\theta)$ is represented by the set of equations (4):

$$h(\theta) < MUCT \wedge \theta < \theta_{MAXi} \quad \Rightarrow \quad A_p(\theta) = A_c(\theta)$$
$$h(\theta) > MUCT \quad \Rightarrow \quad A_p(\theta) = A_{pMAX} \quad (4)$$
$$h(\theta) < MUCT \wedge \theta > \theta_{MAXo} \quad \Rightarrow \quad A_p(\theta) = A_c(\pi) - A_c(\theta)$$

To profitably calibrate the model, two distinguished phases must be accomplished. The initial phase concerns the identification of the MUCT. Its detection is obtained experimentally by machining several channels at constant cutting speed V_C, and depth of cut a_p, while applying different values of f_Z. The acquired cutting forces $F_C(\theta)$ are then normalized respect to the chip cross-sectional area (equation (5)), attaining the Specific Cutting Force (SCF):

$$SCF(\theta) = \frac{F_C(\theta)}{a_p \cdot h(\theta)} = \frac{F_C(\theta)}{a_p \cdot f_Z \cdot sin(\theta)} \quad (5)$$

The typical behavior of SCF during the variation of f_Z is characterized by three different zones [16]. At low f_Z values, SCF is the highest, and it rapidly decrements when f_Z increases; here only the ploughing removal mechanism is present. Increasing again f_Z, a transition zone, is observed. This section is characterized by the coexistence of both ploughing and shearing regimes and shows again a decrement of SCF during the increase of f_Z, even if with a lower slope of the curve. Finally, at higher f_Z, the constancy of SCF is detectable, and the only removal mechanism is shearing; therefore, the amount of f_Z at the beginning of this area can be considered as the MUCT value.

In the second phase of the model development, the optimization of the model coefficients K_{ts}, K_{rs}, K_{tp}, and K_{rp} is performed. In particular, the employed optimization algorithm is the Particle Swarm Optimization (PSO) by Eberhart and Kennedy [17], largely used in the optimization of process parameters for different applications [18, 19]. Following this methodology, an object function, usually an error function to be minimized, must be individuated.

When employing a two flutes mill, F_C shows the occurrence of two peaks, as a function of the tool rotation angle, related to the first and the second cutting edge. The peak forces in the F_c resultant can be defined as $F_{Cmax}(CE1)$ and $F_{Cmax}(CE2)$ for the first and the second cutting edge respectively. An average cutting force peak can be defined as $F_{exp.cMAX}$. It can be compared to the cutting force peak predicted by the analytical model, defined as $F_{model.cMAX}$. The objective function to be minimized is defined by equation (6):

$$Objective\ Function = Err = \sum \left(\frac{|F_{model.cMAX} - F_{exp.cMAX}|}{F_{exp.cMAX}} \right)_i \quad (6)$$

The minimization of the object function Err was performed iteratively by employing a search algorithm. Under this point of view, a great number of values must be tested until finding the optimized coefficients values that minimize the object function. The equations (1)-(6) of the analytical model were implemented in a Matlab® function for calculating the forces and the error Err. An initial set of model parameters K_{ts}, K_{rs}, K_{tp}, and K_{rp} was assumed by the algorithm and the Err evaluation was performed by comparison with experimental data. Following then the restriction related to the modification of the parameters, the algorithm iteratively changes the parameters' values until the minimized value of Err was reached, and the relative optimized model coefficient were identified. As understandable, the procedure is effective only if several experimental data are available. For this reason, an intensive experimental campaign, following described, was performed.

3. Materials and Methods

Concerning the additive manufactured specimens, the raw materials were Ti6AlV4 powders, namely EOS Ti6Al4V. Properties and chemical composition of the atomized powders, as stated by datasheets and accordingly to ASTM B214, B15, B212, F2924 and F1472 standards [20-21], are reported in Table 1. The fabrication of PBF-LB samples has been realized by an EOS M290.

The realized samples have a cubic geometry with an edge length of 10 mm. With respect to the building plate, the designated growing angle was 0°. This strategy has been applied, following the achieved lab experience in using the previously mentioned machines and powders, to reproduce surface characteristics enhancing osseointegration of an implant, without the need of laborious post-processes. The scanning strategy of the PBF-LB machine alternates the angle between each layer of 67°. The employed process parameters for the specimens' building were a laser power of 340 W, a laser focus of 70 μm, a scanning speed of 1250 mm/s, a hatch spacing of 40 μm, and a slice thickness of 30 μm. The stability of the PBF-LB process was ensured by the construction of support structures applying a laser power of 100 W and a scanning speed of 600 mm/s.

Table 1. Properties of employed powders for the PBF-LB.

Powder property	PBF-LB
Particle size analysis (μm)	
d10	27.79
d50	31.18
d90	54.45
Powder apparent density (g/cm³)	2.31
Chemical composition (wt %)	
Al	5.92
V	4.04
O	0.13
Fe	0.20
Ti	Bal.

In order to retain the oxygen contamination of the samples at a percentage value lower than 0.1 %, a controlled argon gas atmosphere was maintained during PBF process. Finally,

supports were removed and specimens were sonically cleaned in an acetone-isopropanol solution before to be let to dry.

The experimental micro-milling campaign was performed by means of a five axis nano-precision machining center KERN Pyramid Nano equipped with a Heidenhain iTCN 530 numeric control. The measurement of the cutting loads was accomplished with a piezoelectric 3-component loadcell (Kistler 9317C) cabled with a charge amplifier (Kistler 5015A), as described in [22,23]. The workpieces were linked to the loadcell which in turn was secured to the machine worktable. To attain a flat surface, a single pass roughing process was carried out by a three-flutes flat bottom mill, with a nominal diameter of 3 mm applying a depth of cut equal to 100 µm, a cutting speed of 100 m/min and a feed of 7.5 µm/tooth. Following this, a coated two-flutes micro mill, with a nominal diameter of 0.5 mm (Fig. 2), was utilized for machining microchannels. In order to prevent possible loadcell damages, the micromachining tests were performed in dry condition. This was moreover indicated by the tool manufacturer in case of lightweight alloys cutting by Titanium Nitride tool coating. The details related to the geometrical characteristics, acquired with the Hirox RH 2000 confocal microscope, and tool materials are summarized in Table 2.

Table 2. Properties of the tool used for the micro slot machining.

Properties	Value
Model	Rime HM79/05
Nominal (µm)	500
Effective diameter (µm)	475°±4[*]
Effective cutting edge radius (µm)	5±2
Helix angle (°)	30
Material	Tungsten Carbide
Coating material	Titanium Nitride

*Measured by the BLUM laser measuring system mounted on the CNC machine

In all the accomplished micromachining tests the tool was shifted starting from the external part of the specimen to its center by maintaining a constant $a_p = 0.03$ mm. Concerning the totality of the cutting experiments, it is possible to divide them into two groups.

A first group of tests was effectuate keeping a constant $V_C = 40$ m/min and by machining eight channels on the samples top surface, varying f_Z in a range from 0.5 µm/tooth to 3.5 µm/tooth. These values were selected experimentally, after observing that the employment of f_Z higher than 5 µm/tooth led to a tool catastrophic breakage. This part of the experimental campaign was developed for measuring the cutting forces in order to evaluate the ploughing-shearing transition respect to the MUCT assessment. The cutting forces related to this set of experiments were acquired permitting to individuate the MUCT and, by applying the PSO algorithm previously described, to calibrate the coefficients of the proposed analytical model for force calculations.

The second group of micro-milling tests was carried out to acquire additional force data for analyzing how the process parameters affect cutting forces, and the related specific loads,

and for validating the developed model, by a comparison between experimental and analytical results. The corresponding experimental plan (Fig. 3) is a centered composite design (CCD), with a total of nine combination of the factors. For statistical reliability, three repetitions of the central point must be performed. Considering the applied CCD, five values of both cutting speed and feed per tooth were implemented, while the depth of cut was maintained constant at a value of 0.03 mm for all the tests.
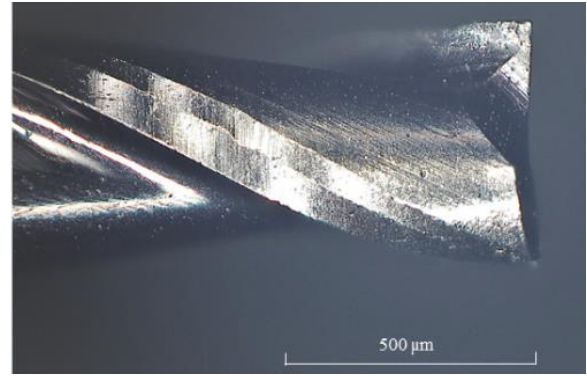
Fig. 2. Example of a micro mill with a diameter of 0.5 mm.

For removing any adherent material from the tool, it was cleaned with a silicone rubber after each test. Moreover, after the cutting of a single sample the tool was replaced. The tool wear was monitored by a digital optical microscope, resulting negligible. The machining load components along every direction, acquired by the force measuring system, were then combined for determining the total cutting force (F_C).

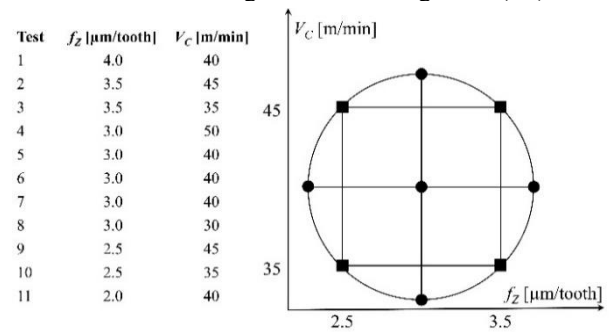| Test	f_Z [µm/tooth]	V_C [m/min]
1	4.0	40
2	3.5	45
3	3.5	35
4	3.0	50
5	3.0	40
6	3.0	40
7	3.0	40
8	3.0	30
9	2.5	45
10	2.5	35
11	2.0	40

Fig. 3. Levels of the process parameters implemented in the CCD plan.

4. Results and Discussion

The proposed analytical model was calibrated by considering the forces acquired during the first group of tests, performed at constant speed and with decreasing feed rate. Firstly, the model tuning requires the identification of MUCT parameter by considering the trend of the SCF peaks as the feed per tooth decreases. The dependence of the SCF on feed per tooth is highlighted in Fig. 4. The force peak is reached at the maximum value of chip cross-sectional area, corresponding to the maximum value of $h(\theta)$, when θ is equal to $\pi/2$ rad. At this angle $h(\theta) = f_Z$, thus the assessment of MUCT, by the analysis of Fig. 4, can be performed considering f_Z in stead of $h(\theta)$ without mistakes.
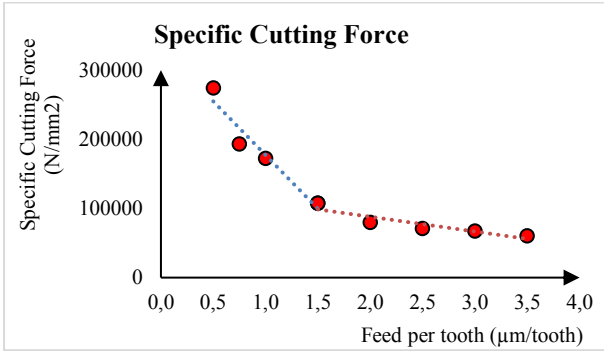
Fig. 4. Specific Cutting Force value as function of feed per tooth.

The pressure on the tool edge decreases as feed per tooth increases and a meaningful change of slope is visible at 1.5 μm/tooth, which was considered as the value for MUCT in the model calibration. The calibration procedure was performed by considering a domain for parameters K_{ts} and K_{rs} equal to [0;100000], while for parameters K_{tp}, and K_{rp} the domain was considered equal to [0;1000000].

The PSO algorithm was set with a population of 100 particles and a number of iterations equal to 1000. The algorithm was run ten times in order to find a better solution. In the best iteration, the function *Err* defined by Eq. 6 resulted equal to 0.731. The calibrated model is defined by Eq. 7:

$$F_t(\theta) = \left(61543 \cdot h(\theta) + 519097 \cdot A_p(\theta)\right) \cdot a_p$$
$$F_r(\theta) = \left(79479 \cdot h(\theta) + 733193 \cdot A_p(\theta)\right) \cdot a_p \tag{7}$$

The model well fits the experimental data, regardless the feed rate. The experimental cutting force signal shows a good balance between the two tool flutes due to a low tool run out. The percentage error on the cutting force peak prediction oscillates between a minimum of 0.00% (Test f_z=0.75 μm/tooth) and a maximum of 28.5% (Test f_z=0.50 μm/tooth). The average percentage error was calculated as the mean of the percentage error of each test, and it resulted equal to 9.14%. It can be considered a good result having regard of the high extension of the domain of the feed rate, which covers both ploughing and shearing regimes.

Fig. 5 and Fig. 6 shows two examples of comparison between experimental data (as average of thirty cutting tool rotations) and the model. The remaining six tests show analogue trends. The model well fits the signal around the cutting force peaks, while the shape of the curve is different where the cut begins and ends. When ploughing regime is dominant, the model predicts a cutting force sharper then the experimental data. The experimental cutting force results smoother, and the model generally underestimates the signal.

Further tests were performed by following a CCD experimental plan, by changing feed per tooth and cutting speed on five different levels. The experimental cutting force were collected in order to evaluate the dynamics effects of the cutting and to validate the calibrated analytical model. During the experimental tests with different cutting speed the tool run-out increased and only one tool flute was engaged with workpiece. The phenomena of tool run-out is a random effect and it was in complete opposition with the results of the constant cutting speed tests.
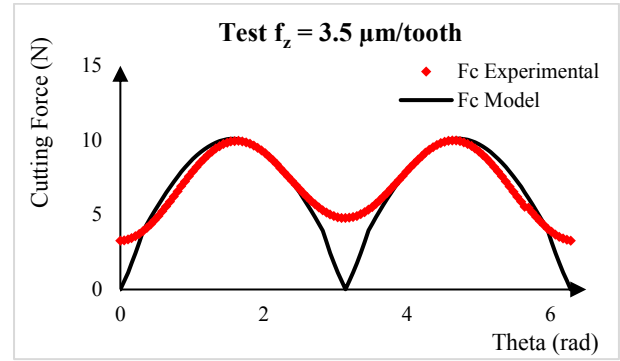

Fig. 5. Comparison between the experimental signal of cutting force and the model prediction for test with feed per tooth equal to 3.5 μm/tooth.
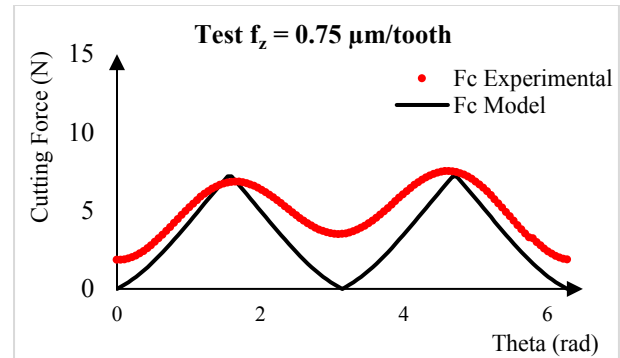

Fig. 6. Comparison between the experimental signal of cutting force and the model prediction for test with feed per tooth equal to 0.75 μm/tooth.

However, the model described by Eq. 7 ensured a good prediction also in this condition. The average error about the prediction of the maximum cutting force resulted equal to 6.05%. The error oscillates between a minimum of 1.1 % for the test with a cutting speed of 45 m/min and a feed per tooth of 2.5 μm/tooth, and a maximum of 21.4% for the test with the maximum cutting speed (40 m/min) and the maximum feed per tooth (4.0 μm/tooth). The complete results are listed in Table 3.

Table 3. Percentage error of the model prediction.

Test ID	f_z (mm/rev)	v_c (m/min)	Err (%)
1	0,0040	40	21,4
2	0,0035	45	6,3
3	0,0035	35	2,9
4	0,0030	50	1,2
5	0,0030	40	6,4
6	0,0030	40	3,1
7	0,0030	40	6,2
8	0,0030	30	2,5
9	0,0025	45	1,1
10	0,0025	35	8,4
11	0,0020	40	7,2

Fig. 7 and Fig. 8 show an example of the comparison between the experimental data and the model prediction. The cutting force exhibits only one peak due to the run-out effect which determines the engagement of only one tool flute with the workpiece. The transition between ploughing and shearing

regimes is marked by a sharp edge in the predicted curvature, as visible in Fig. 7. When ploughing become more relevant, the peak of the predicted cutting force is less smooth, and the concavity is not according with the experimental data.
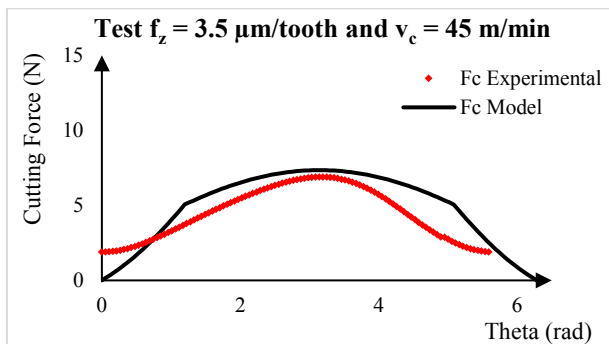

Fig. 7. Comparison between the experimental signal and the model prediction for test with f_z = 3.5 µm/tooth and v_c = 45 m/min.
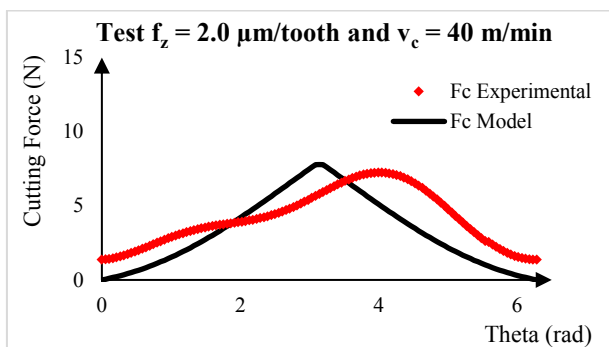

Fig. 8. Comparison between the experimental signal and the model prediction for test with f_z = 2.0 µm/tooth and v_c = 40 m/min.

5. Conclusion

The authors investigated the micro-machinability of Ti64 alloy samples fabricated by L-PBF process. The experimental analysis favourites the embedding between micro milling and additive manufacturing in order to integrate their respective advantages. An analytical model was successfully calibrated by considering the cutting regime transition, a key feature of micro machining processes. The model tuning required the computation of the Minimum Uncut Chip Thickness and the calculation of the unknown parameters of the model through PSO algorithm. The model was subsequently applied to predict the cutting force measured during microchannel performed by following an experimental CCD full factorial plan. A good matching between experimental data and model prediction was finally achieved as the major research output.

References

[1] Plessis A, Yadroitsava I, Yadroitsev I. Effects of defects on mechanical properties in metal additive manufacturing: A review focusing on X-ray tomography insight. Mater Des 2020;187:108385.

[2] Melia MA, Duran JG, Koepke JR, Saiz DJ, Jared BH, Schindelholz EJ. How build angle and post-processing impact roughness and corrosion of additively manufactured 316L stainless steel. Mater Degrad 2020; 4(21).

[3] Lou S, Jiang X, Sun W, Zeng W, Pagani L, Scott PJ. Characterisation methods for powder bed fusion processed surface topography. Precis Eng 2019;57:1-15.

[4] Li J, Cui X, Hooper GJ, Lim KS, Woodfield TBF. Rational design, bio-functionalization and biological performance of hybrid additive manufactured titanium implants for orthopaedic applications: A review. J. Mech Behav Biomed Mater 2020;105:103671.

[5] Ginestra P, Ceretti E, Lobo D, Lowther M, Cruchley S, Kuehne S, Villapun V, Cox S, Grover L, Shepherd D, Attallah M, Addison O, Webber M. Post processing of 3D printed metal scaffolds: A preliminary study of antimicrobial efficiency. Procedia Manuf 2020;47:1106-1112.

[6] Ginestra P, Riva L, Ceretti E, Lobo D, Mountcastle S, Villapun V, Cox S, Grover L, Attallah M, Addison O, Shepherd D, Webber M. Surface finish of additively manufactured metals: Biofilm formation and cellular attachment. ESAFORM 2021 - 24th International Conference on Material Forming 2021 art. no. 2089.

[7] Ginestra P, Ferraro RM, Zohar-Hauber K, Abeni A, Giliani S, Ceretti E. Selective laser melting and electron beam melting of Ti6Al4V for orthopedic applications: A comparative study on the applied building direction. Materials 2020;13(23):5584.

[8] Allegri G, Colpani A, Ginestra PS, Attanasio A. An experimental study on micro-milling of a medical grade Co-Cr-Mo alloy produced by selective laser melting. Materials 2019;12(13): 2208.

[9] Abeni A, Ginestra PS, Attanasio A. Micro-milling of Selective Laser Melted Stainless Steel. In: Ceretti E, Tollio T, editors. Lect Notes Mech Eng. Selected topics in manufacturing. Switzerland: Springer; 2021. P. 1-12.

[10] Wang H, Zhao B, Liu C, Wang C, Tan X, Hu M. A comparison of biocompatibility of a titanium alloy fabricated by electron beam melting and selective laser melting. PLoS ONE 2016;11(7): e0158513.

[11] Rafi HK, Karthik NV, Gong H, Starr TL, Stucker BE. Microstructures and mechanical properties of Ti6Al4V parts fabricated by selective laser melting and electron beam melting. J. Mater Eng Perform 2013;22(12):3872-3883.

[12] Koike M, Greer P, Owen K, Lilly G, Murr LE, Gaytan SM, Martinez E, Okabe T. Evaluation of titanium alloys fabricated using rapid prototyping technologies-electron beam melting and laser beam melting. Materials 2011;4(10):1776-1792.

[13] Abeni A, Ginestra PS, Attanasio A. Comparison Between Micro Machining of Additively Manufactured and Conventionally Formed Samples of Ti6Al4V Alloy. In: Ceretti E, Tollio T, editors. Lect Notes Mech Eng. Selected topics in manufacturing. Switzerland: Springer; 2020. p. 91-106.

[14] Malekian M, Mostofa MG, Park SS, Jun MBG. Modeling of minimum uncut chip thickness in micro machining of aluminum. J. Mater Process Technol 2012;212(3):553-559.

[15] Rivière-Lorphèvre E, Letot C, Ducobu F, Dehombreux P, Filippi E. Dynamic simulation of milling operations with small diameter milling cutters: effect of material heterogeneity on the cutting force model. Meccanica 2017;52(1):35-44.

[16] Abeni A, Loda D, Özel T, Attanasio A. Analytical force modelling for micro milling additively fabricated Inconel 625. Prod Eng 2020;14(5-6):613-627.

[17] Eberhart R, Kennedy J. A new optimizer using particle swarm theory. In: Proceedings of the Sixth International Symposium on Micro Machine and Human Science. Nagoja: IEEE; 1995. p. 39-43.

[18] Raja SB, Baskar N. Particle swarm optimization technique for determining optimal machining parameters of different work piece materials in turning operations. Int J. Adv Manuf Technol 2011;54(5-8):445-463.

[19] Ciurana J, Arias G, Özel T. Neural network modeling and particle swarm optimization (PSO) of process parameters in pulsed laser micromachining of hardenend AISI H13 steel. Mater Manuf Process 2009;24(3):358-368.

[20] ASTM B214-16 Standard Test Method for Sieve Analysis of Metal Powders ASTM: West Conshohocken, PA, USA, 2016; Volume 02.05 .

[21] ASTM F2924-14 Standard Specification for Additive Manufacturing Titanium-6 Aluminum-4 Vanadium with Powder Bed Fusion ASTM: West Conshohocken, PA, USA, 2014; Volume 10.04.

[22] Attanasio A, Abeni A, Özel T, Ceretti E. Finite element simulation of high speed micro milling in the presence of tool run-out with experimental validations. Int J. Adv Manuf Technol 2019;100(1-4):25-35.

[23] Abeni A, Metelli A, Cappellini C, Attanasio A. Experimental Optimization of Process Parameters in CuNi18Zn20 Micromachining. Micromachines 2021;12(11):1293.